Investigation of two-fluid methods for Large Eddy Simulation of spray combustion in Gas Turbines

Boileau M.[1], Pascaud S.[2], Riber E.[1−3], Cuenot B.[1],

Gicquel L.Y.M.[1] and Poinsot T.J.[3]

October 29, 2007

[1]*CERFACS, 42 avenue Gaspard Coriolis, 31057 Toulouse Cedex 01, France*

[2] *Now at TURBOMECA (Safran Group), Pau, France*

[3]*IMFT (UMR CNRS-INPT-UPS 5502), Toulouse, France*

Abstract

An extension of the Large Eddy Simulation (LES) technique to two-phase reacting flows, required to capture and predict the behavior of industrial burners, is presented.

While most efforts reported in the literature to construct LES solvers for two-phase flow focus on Euler-Lagrange formulation, the present work explores a different solution ('two-fluid' approach) where an Eulerian formulation is used for the liquid phase and coupled with the LES solver of the gas phase. The equations used for each phase and the coupling terms are presented before describing validation in two simple cases which gather some of the specificities of real combustion chamber: (1) a one-dimensional laminar JP10/air flame and (2) a non-reacting swirled flow where solid particles disperse [1]. After these validations, the LES tool is applied to a realistic aircraft combustion chamber to study both a steady flame regime and an ignition sequence by a spark. Results bring new insights into the physics of these complex flames and demonstrate the capabilities of two-fluid LES.

Keywords: Spray combustion, Turbulence, Large Eddy Simulation, Gas turbines.

1 Introduction

RANS (Reynolds Averaged Navier Stokes) equations are routinely solved to design combustion chambers, for both gaseous and liquid fuels. Recently, in order to provide better accuracy for the prediction of mean flows but also to give access to unsteady phenomena occurring in combustion devices (such as ignition, instabilities, flashback or quenching), Large-Eddy Simulation (LES) has been extended to reacting flows. As shown by the numerous examples published in the last years [2–12], this approach is very accurate in complex turbulent gaseous flows. This mainly results from the explicit and direct computation of the largest scale structures of the flow, which are the most difficult to model and contain a significant part of the physics controlling the flame.

However most LES calculations consider only gaseous flows and flames. The introduction of a dispersed liquid fuel raises two kinds of problems:

- The physics of a liquid fuel spray is very complex and is not yet fully understood [13]. The atomization process of a liquid fuel jet [14–18], the turbulent dispersion of the resulting droplets [19–23], their interaction with walls [24, 25], their evaporation and combustion [26] are phenomena occuring for LES at the subgrid scale and therefore requiring accurate modelling.

- The numerical implementation of two-phase flow in LES remains a challenge. The equations for both gaseous and dispersed phases must be solved together at each time step in a strongly coupled manner. This differs again from classical RANS where both phases can be solved in a weakly coupled procedure, bringing first the gas flow to convergence, then calculating the associated dispersed phase and iterating until convergence of both phases.

Attempts to extend RANS formulation to LES of two-phase combustion may be found in [7, 27–30]. They are all based on a Euler-Lagrange (EL) description of

3

the dispersed phase in which the flow is solved using an Eulerian method and the particles are tracked with a Lagrangian approach. An alternative is the Euler-Euler (EE) description, also called two-fluid approach, in which both the gas and the dispersed phases are solved using an Eulerian formulation.

In RANS codes, the weak numerical coupling of the phases makes the EL method well suited for gas turbine computations, but RANS with the EE approach may also be found for example in simulations of fluidized beds [31,32] or chemical reactors [33–35], two examples of two-phase flows with a high load of particles. The experience gained in the development of RANS has led to the conclusions that both approaches are useful and they are both found today in most commercial codes. Moreover, coupling strategies between EE and EL methods within the same application are considered for certain cases. In the framework of LES of gas turbines, it is interesting to compare again EL or EE formulations.

Following the individual trajectory of millions of droplets created by standard injectors implies computer resources that are still far beyond the capacities of computers available today and even in the coming years. To overcome this problem the stochastic Lagrangian approach is usually introduced, where each particle is only a "numerical" particle, representing in fact a statistically homogeneous group of real particles. This reduces the number of particles to compute but implies modelling for these parcels of particles [36]. Moreover in order to reach the accuracy required by LES, the stochastic Lagrangian approach must still involve an important number of particles that make it CPU time-consuming. Another difficult point is that the topology of the flow in dense zones (like near the injectors) differs from a cloud of droplets and a Lagrangian description is not adapted there. Finally the computer implementation of the EL approach is not well-suited to parallel computers: since two different solvers must be coupled, the complexity of the implementation on a parallel computer increases drastically compared to a single-phase code. Two

methods may be used for LES: (1) task parallelization in which certain processors compute the gas flow and others compute the droplets flow and (2) domain partitioning in which droplets are computed together with the gas flow on geometrical subdomains mapped on parallel processors. Droplets must then be exchanged between processors when leaving a subdomain to enter an adjacent domain. For LES, it is easy to show that only domain partitioning is efficient on large grids because task parallelization would require the communication of very large three-dimensional data sets at each iteration between all processors. However, codes based on domain partitioning are difficult to optimize on massively parallel architectures when droplets are clustered in one part of the domain (typically, near the fuel injectors). Moreover, the distribution of droplets may change during the computation: for a gas turbine re-ignition sequence, for example, the chamber is filled with droplets when the ignition begins thus ensuring an almost uniform droplet distribution; these droplets then evaporate rapidly during the computation, leaving droplets only in the near injector regions. To preserve a high parallel efficiency on thousands of processors, dynamic load-balancing strategies are required that re-decompose the domain during the computation itself [30].

The EE approach has the important advantage to be straightforward to implement in a numerical tool, and immediately efficient as it allows the use of the same parallel algorithm than for the gas phase [37]. However it requires an initial modelling effort much larger than in the EL method [38] and faces difficulties in handling droplet clouds with extended size distributions [39]. Moreover the resulting set of equations is numerically difficult to handle and requires special care [40].

Throughout this paper, two-phase flows will be treated like monodisperse sprays, an assumption which is not mandatory in EE methods but which makes their implementation easier. Results also suggest that in many flows (see for example section 4), this assumption is reasonable. Considering the lack of information on size

5

distribution at an atomizer outlet in a real gas turbine, this assumption might be a reasonable compromise in terms of complexity and efficiency: tracking multi-disperse sprays with precision makes sense only if the spray characteristics at the injection point are well known. In most cases, droplets are not yet formed close to the atomizer outlet anyway and even the Lagrange description faces difficulties there.

In the context of LES, a new modelling issue appears for two-phase flow simulations, either in the EL or EE formulation, and is linked to the subgrid scale model for the turbulent droplet dispersion. This problem has already been addressed in [41, 42] but is still an open question. However in the case of reacting flows, turbulent droplet dispersion occurs in a very limited zone between the atomizer and the flame and it is greatly influenced by the flame dynamics, therefore limiting the impact of the subgrid scale model.

The EE methodology in LES used throughout this work is taken from previous work [38, 40, 43, 44] where the validity and limitations have been discussed extensively, and it is not the purpose here to discuss further theoretical aspects. Despite the known limitations of such methodology, it is interesting to evaluate the potential and accuracy of the existing models when applied to realistic geometries and flows. This is the objective of the present paper, in the case of aeronautical gas turbines.

The framework and the basic equations for the EE description are first recalled in Section 2. The LES filtering procedure for these equations is described in Section 2.5 along with the closure assumptions and models for subgrid terms, including turbulent combustion. Simple validation cases are then presented: the laminar two-phase one-dimensional flame and the dispersion of particles in a turbulent swirled flow [1] are described in Section 3 and Section 4 respectively. The final application is a sector of a gas turbine burner for which both the steady flow and

an ignition sequence using a spark discharge are computed in Sections 5.2 and 5.3 respectively.

2 Equations

2.1 Carrier phase

The set of instantaneous conservation equations in a multi-species reacting gas can be written:

$$\frac{\partial \mathbf{w}}{\partial t} + \nabla \cdot \mathbf{F} = \mathbf{S_c} + \mathbf{S_l} \tag{1}$$

where $\mathbf{w}$ is the vector of the gaseous conservative variables $\mathbf{w} = (\rho u, \rho v, \rho w, \rho E, \rho_k)^T$ with respectively ρ, u, v, w, E, ρ_k the density, the three Cartesian components of the velocity vector $\mathbf{u} = (u, v, w)^T$, the total energy per unit mass defined by $E = \frac{1}{2}\mathbf{u} \cdot \mathbf{u} + E_i$ where E_i is the internal energy, and $\rho_k = \rho Y_k$ where Y_k is the mass fraction of species k. It is usual to decompose the flux tensor $\mathbf{F}$ into an inviscid and a viscous component: $\mathbf{F} = \mathbf{F}(\mathbf{w})^I + \mathbf{F}(\mathbf{w}, \nabla \mathbf{w})^V$. The three spatial components of the inviscid flux tensor $\mathbf{F}(\mathbf{w})^\mathbf{I}$ are:

$$\begin{pmatrix} \rho u^2 + P & \rho uv & \rho uw \\ \rho uv & \rho v^2 + P & \rho vw \\ \rho uw & \rho vw & \rho w^2 + P \\ (\rho E + P)u & (\rho E + P)v & (\rho E + P)w \\ \rho_k u & \rho_k v & \rho_k w \end{pmatrix} \tag{2}$$

where the hydrostatic pressure P is given by the equation of state for a perfect gas: $P = \rho r T$, with the gas constant $r = \frac{R}{W} = \sum_{k=1}^{N} \frac{Y_k}{W_k}\mathcal{R}$ and $\mathcal{R} = 8.3143$ J/(mol.K) the universal gas constant. The internal energy E_i is linked to the temperature through the heat capacity of the mixture calculated as $C_p = \sum_{k=1}^{N} Y_k\, C_{p,k}$.

7

The components of the viscous flux tensor $\mathbf{F}(\mathbf{w}, \nabla\mathbf{w})^V$ take the form:

$$
\begin{pmatrix}
-\tau_{xx} & -\tau_{xy} & -\tau_{xz} \\
-\tau_{xy} & -\tau_{yy} & -\tau_{yz} \\
-\tau_{xz} & -\tau_{yz} & -\tau_{zz} \\
-\mathbf{u}\cdot\tau_x + q_x & -\mathbf{u}\cdot\tau_y + q_y & -\mathbf{u}\cdot\tau_z + q_z \\
J_{x,k} & J_{y,k} & J_{z,k}
\end{pmatrix}
\tag{3}
$$

It is composed of the stress tensor $\tau = 2\mu(S - 1/3 \ \delta_{ij}Tr(S))$ (momentum equations), the energy flux $\mathbf{u}\cdot\tau + q$ (energy equation) and the diffusive flux J_k (species equations). In the stress tensor expression, $S = 1/2(\nabla\cdot\mathbf{u} + (\nabla\cdot\mathbf{u})^T)$ is the deformation matrix and μ is the dynamic viscosity following a classical power law. The diffusive flux of species k includes a correction velocity V^c that guarantees mass conservation, so that $J_k = -\rho\left(D_k\frac{W_k}{W}\nabla X_k - Y_k V^c\right)$ with $V^c = \sum_{k=1}^{N} D_k\frac{W_k}{W}\nabla X_k$, X_k being the molar fraction of species k. The mixture diffusion coefficient for species k is computed as $D_k = \frac{\mu}{\rho Sc_k}$ where the Schmidt number Sc_k is a constant. Finally the heat flux vector q follows a Fourier's law and includes an additional term due to heat transport by species diffusion: $q = -\lambda\nabla T + \sum_{k=1}^{N} J_k h_{s,k}$, where $\lambda = \mu C_p/Pr$ is the heat conduction coefficient of the mixture, with the Prandtl number Pr fixed at a constant value.

The chemical part of the source term $\mathbf{S_c}$ on the right hand side of Eq. (1) adds a term to the energy equation ($\dot{\omega}_T$) and to the species equations ($\dot{\omega}_k$). Chemistry is described by M reactions involving the N reactants $\mathcal{M}_k$ as follows:

$$
\sum_{k=1}^{N} \nu'_{kj}\mathcal{M}_k \rightleftharpoons \sum_{k=1}^{N} \nu''_{kj}\mathcal{M}_k, \qquad j = 1, M
\tag{4}
$$

The production/consumption rate $\dot{\omega}_k$ for species k is the sum of the reaction rates $\dot{\omega}_{kj}$ produced by all M reactions:

$$
\dot{\omega}_k = \sum_{j=1}^{M} \dot{\omega}_{kj} = W_k \sum_{j=1}^{M} \nu_{kj}\mathcal{Q}_j
\tag{5}
$$

where $\nu_{kj} = \nu''_{kj} - \nu'_{kj}$ and $\mathcal{Q}_j$ is the rate of progress of reaction j and is written:

$$\mathcal{Q}_j = K_{f,j} \prod_{k=1}^{N} \left(\frac{\rho Y_k}{W_k} \right)^{\nu'_{kj}} - K_{r,j} \prod_{k=1}^{N} \left(\frac{\rho Y_k}{W_k} \right)^{\nu''_{kj}} \tag{6}$$

The forward reaction rate follows an Arrhenius law: $K_{f,j} = A_{f,j} \exp\left(-\frac{E_{a,j}}{\mathcal{R}T}\right)$ where $A_{f,j}$ and $E_{a,j}$ are the pre-exponential factor and the activation energy. The reverse reaction rate is deduced from the equilibrium relation $K_{r,j} = K_{f,j}/K_{eq}$ where K_{eq} is the equilibrium constant.

The heat release is calculated from the species production/consumption rates as:

$$\dot{\omega}_T = -\sum_{k=1}^{N} \dot{\omega}_k \Delta h^0_{f,k} \tag{7}$$

where $\Delta h^0_{f,k}$ is the formation enthalpy of species k.

The second part of the source term $\mathbf{S_l}$ is associated to the liquid phase through the drag force and the evaporation. It adds a vector I to the right hand side of the momentum equations, a heat transfer term Π on the energy equation and a mass transfer term Γ on the fuel equation (see Section 2.3).

2.2 Dispersed phase

Eulerian equations for the dispersed phase may be derived by several means. A popular and simple way consists in volume filtering of the separate, local, instantaneous phase equations accounting for the inter-facial jump conditions [45]. Such an averaging approach may be restrictive, because particle sizes and particle distances have to be smaller than the smallest length scale of the turbulence. Besides, it does not account for the Random Uncorrelated Motion (RUM), which measures the deviation of particles velocities compared to the local mean velocity of the dispersed phase [38] (see section 2.4). In the present study, a statistical approach analogous to kinetic theory [46] is used to construct a probability density function (pdf) $\breve{f}_p(\mathbf{c}_p, \zeta_p, \mu_p, \mathbf{x}, t)$ which gives the local instantaneous probable number of

9

droplets with the given translation velocity $\mathbf{u}_p = \mathbf{c}_p$, the given mass $m_p = \mu_p$ and the given temperature $T_p = \zeta_p$. The resulting model leads to conservation equations having the same form than for the gas phase, for the particle number density $\breve{n}_l$, the volume fraction $\breve{\alpha}_l$, the correlated velocity $\breve{u}_l$ (see section 2.4) and the sensible enthalpy $\breve{h}_{s,l}$ (supposed uniform in the droplet, so that in particular the interface temperature T_ζ is equal to the liquid temperature T_l). For a monodisperse spray, neglecting droplets interaction terms, the conservation equations read:

$$\frac{\partial}{\partial t}\breve{n}_l \;+\; \frac{\partial}{\partial x_j}\breve{n}_l \breve{u}_{l,j} = 0 \tag{8}$$

$$\frac{\partial}{\partial t}\rho_l \breve{\alpha}_l \;+\; \frac{\partial}{\partial x_j}\rho_l \breve{\alpha}_l \breve{u}_{l,j} = -\Gamma \tag{9}$$

$$\frac{\partial}{\partial t}\rho_l \breve{\alpha}_l \breve{u}_{l,i} \;+\; \frac{\partial}{\partial x_j}\rho_l \breve{\alpha}_l \breve{u}_{l,i}\breve{u}_{l,j} = F_{d,i} - \breve{u}_{l,i}\Gamma - \frac{\partial}{\partial x_j}\rho_l \breve{\alpha}_l \delta \breve{R}_{l,ij} \tag{10}$$

$$\frac{\partial}{\partial t}\rho_l \breve{\alpha}_l \breve{h}_{s,l} \;+\; \frac{\partial}{\partial x_j}\rho_l \breve{\alpha}_l \breve{h}_{s,l}\breve{u}_{l,j} = -(\Phi + \Gamma h_{s,F}(\breve{T}_l)) \tag{11}$$

In these equations, the momentum and heat phase exchange source terms are split in two parts : $I = -F_d + \breve{\mathbf{u}}_l\Gamma$ includes both the drag force and a momentum transfer due to the mass transfer, and $\Pi = \Phi + \Gamma h_{s,F}(\breve{T}_l)$, where $h_{s,F}(\breve{T}_l)$ is the fuel vapor enthalpy taken at the interface temperature T_l, includes conduction and heat transfer linked to the mass transfer. The tensor $\delta \breve{R}_{l,ij}$ corresponds to the random uncorrelated motion (RUM) and is explained in section 2.4.

Note that without source terms (i.e. without evaporation, drag and RUM) the momentum equation Eq. 10 is similar to the Burger's equation, known to create shock-like velocity gradients and therefore difficult to handle numerically. The absence of an isotropic pressure-like force can also lead to very high droplet number density gradients. Such behaviors are unphysical and should be avoided. To this purpose it is necessary to add stabilisation terms to this equation. This is explained in section 2.6. Consequently the final Eulerian model without RUM is strictly valid only for small Stokes number droplets, that behave like tracers and do not form sharp number density gradients.

It has been shown in [47] that the resulting set of equations Eqs. 8 to 11 leads to solutions similar to Lagrangian solutions in the case of a two-phase turbulent channel flow.

2.3 Phase exchange source terms

Mass transfer between the gas and the liquid phases is linked to evaporation, which follows the classical Spalding model [48]. Assuming that the dispersed phase is composed of spherical droplets of pure fuel (denoted with the subscript F), the evaporation rate may be written as :

$$\Gamma = \pi \breve{n}_l d Sh (\rho D_F) ln(1 + B_M) \tag{12}$$

where d is the droplet diameter, D_F is the fuel vapor diffusivity and Sh is the Sherwood number that takes into account convective and turbulent effects. A commonly used expression for this number is $Sh = 2.0 + 0.55 Re_d^{1/2} Sc_F^{1/3}$ where $Re_p = d|\mathbf{u} - \breve{\mathbf{u}}_l|/\nu$ is the particle Reynolds number and Sc_F is the fuel vapor Schmidt number. In this definition ν is the carrier phase kinematic viscosity. In Eq. (12), one important parameter is the Spalding number $B_M = (Y_{F,\zeta} - Y_F)/(1 - Y_{F,\zeta})$ where $Y_{F,\zeta}$ is the fuel mass fraction at the droplet surface, calculated from the fuel vapor partial pressure at the interface $p_{F,\zeta}$ which is evaluated from the Clausius-Clapeyron relation:

$$p_{F,\zeta} = p_{cc} \, exp \left(\frac{W_F L_v}{\mathcal{R}} \left(\frac{1}{T_{cc}} - \frac{1}{T_l} \right) \right) \tag{13}$$

The reference pressure and temperature p_{cc} and T_{cc} correspond to the saturation conditions, and L_v is the latent heat of vaporisation.

The drag force is expressed as:

$$F_d = \frac{\rho_l \breve{\alpha}_l}{\tau_p} \left(u_i - \breve{u}_{l,i} \right) \tag{14}$$

introducing the particle relaxation time τ_p:

$$\tau_p = \frac{4\rho_l d^2}{3\rho\nu C_d Re_d} \tag{15}$$

itself based on the drag coefficient C_d, which is 0.44 for Re_d greater than 1000 and is defined by $C_d = \frac{24}{Re_d}(1 + 0.15\ Re_d^{0.687})$ otherwise.

Finally, the conductive flux Φ through the interface is calculated as $\Phi = \pi \breve{n}_l d\lambda\ Nu(\breve{T}_l - T)$. In this expression, λ is the carrier phase conductivity and Nu is the Nusselt number usually expressed similarly to the Sherwood number: $Nu = 2.0 + 0.55 Re_d^{1/2} Pr^{1/3}$.

2.4 The Random Uncorrelated Motion (RUM)

The averaging operation for the liquid droplet velocity described in the previous section introduces a particle velocity deviation from the mean (or correlated) velocity, noted $u_p'' = u_p - \breve{u}_l$, and named the random uncorrelated velocity [38]. By definition the statistical average (based on the particle probability density function) of this uncorrelated velocity is zero: $< u_p'' >= 0$. A conservation equation can be written for the associated kinetic energy $\delta\breve{\theta}_l =< u_{p,i}'' u_{p,i}'' > /2$:

$$\frac{\partial}{\partial t}\rho_l \breve{\alpha}_l \delta\breve{\theta}_l + \frac{\partial}{\partial x_j}\rho_l \breve{\alpha}_l \breve{u}_{l,j}\delta\breve{\theta}_l = -\frac{1}{2}\frac{\partial}{\partial x_j}\rho_l \breve{\alpha}_l \delta\breve{S}_{l,iij} - \frac{2\breve{n}_l}{\tau_p}\delta\breve{\theta}_l$$
$$- \rho_l \breve{\alpha}_l \delta\breve{R}_{l,ij}\frac{\partial \breve{u}_{l,i}}{\partial x_j} - \Gamma\delta\breve{\theta}_l \tag{16}$$

where unclosed terms $\delta\breve{R}_{l,ij}$ and $\delta\breve{S}_l$ (called here RUM terms) appear. However the modelling of these terms as proposed for example in [47, 49, 50] is not yet satisfactory and it is still an open and difficult question. In [47, 50] it has been shown that in a configuration representative of industrial flows, the RUM is not essential to capture the mean fields (velocity and mass flux) of the liquid phase, but only influences the particle turbulent agitation. It has been therefore omitted in the applications presented later in the paper.

2.5 LES approach

The two sets of conservative equations defined by Eq. (1) and Eqs. (8)-(11) describe turbulent reacting two-phase flows that require a high grid resolution in order to solve from the smallest to the largest scales. In LES only the largest scales are computed while the smallest scales are modelled. A spatially localized time independent filter of given size, $\triangle$, is applied to a single realization of the flow.

The filtered quantity $\overline{f}$ is resolved in the numerical simulation whereas $f' = f - \overline{f}$ is the subgrid scale part due to the unresolved flow motion. For variable density ρ, a mass-weighted Favre filtering is introduced so that:

$$\overline{\rho}\widetilde{f} = \overline{\rho f} \tag{17}$$

The balance equations for gas phase LES are obtained by filtering the instantaneous balance equation (1):

$$\frac{\partial \overline{\mathbf{w}}}{\partial t} + \nabla \cdot \overline{\mathbf{F}} = \overline{\mathbf{S}_{\mathbf{c}}} + \overline{\mathbf{S}_{\mathbf{l}}} \tag{18}$$

where the filtered flux tensor $\overline{\mathbf{F}}$ can be divided in three parts: the inviscid part $\overline{\mathbf{F}}^I$, the viscous part $\overline{\mathbf{F}}^V$ and the subgrid scale turbulent part $\overline{\mathbf{F}}^t$. The three spatial components of the inviscid and viscous flux tensor use expressions similar to Eqs. 2 and 3, based on filtered quantities. The subgrid-scale turbulent flux $\overline{\mathbf{F}}^t = \overline{\tau}^t$ is a new term introduced by the LES approach and is modelled through the turbulent viscosity concept:

$$\overline{\tau}^t = -\overline{\rho}(\widetilde{\mathbf{u} : \mathbf{u}} - \widetilde{\mathbf{u}} : \widetilde{\mathbf{u}}) = 2\,\overline{\rho}\,\nu_t(\widetilde{S} - \frac{1}{3}\delta_{ij}Tr(\widetilde{S})) \tag{19}$$

The turbulent viscosity ν_t is determined using the WALE model [51], similar to the Smagorinsky model, but with an improved behavior near solid boundaries. Similarly, a subgrid-scale diffusive flux vector for species $\overline{J_k}^t = \overline{\rho}\left(\widetilde{\mathbf{u}Y_k} - \widetilde{\mathbf{u}}\widetilde{Y_k}\right)$ and a subgrid-scale heat flux vector $\overline{q}^t = \overline{\rho}(\widetilde{\mathbf{u}E} - \widetilde{\mathbf{u}}\widetilde{E})$ appear and are modelled following the same expressions as in section 2, using filtered quantities and introducing a

13

turbulent diffusivity $D_k^t = \nu_t/Sc_k^t$ and a thermal diffusivity $\lambda_t = \mu_t \overline{C_p}/Pr^t$. The turbulent Schmidt and Prandtl numbers are fixed to 1 and 0.9 respectively.

In turbulent reacting cases the Dynamically Thickened Flame model [52–55] is used, where a thickening factor F is introduced to thicken the flame front and the efficiency function $\mathcal{E}$ developed by Colin *et al.* [4] is used to account for subgrid scale wrinkling.

For the dispersed phase, filtered conservative variables and equations are built with the same methodology as for the carrier phase and similarly a particle subgrid stress tensor $\overline{\tau}_{l,ij}^t$ appears :

$$\overline{\tau}_{l,ij}^t = -\bar{n}_l(\widehat{u_{l,i}u_{l,j}} - \hat{u}_{l,i}\hat{u}_{l,j}) \tag{20}$$

where the Favre filtered quantities $\hat{f}_l$ are defined as $\bar{n}_l\hat{f}_l = \overline{\breve{n}_l\breve{f}_l}$. By analogy to compressible single phase flows [56, 57], Riber et al. propose a viscosity model for the SGS tensor $T_{l,ij}$ [44]. The trace-free SGS tensor is modeled using a viscosity assumption (compressible Smagorinsky model), while the subgrid energy is parametrized by a Yoshizawa model [58] :

$$\overline{\tau}_{l,ij}^t = C_{S,l}2\Delta^2\bar{n}_l|\hat{S}_l|(\hat{S}_{l,ij} - \frac{\delta_{ij}}{3}\hat{S}_{l,kk}) - C_{V,l}2\Delta^2\bar{n}_l|\hat{S}_l|^2\delta_{ij} \tag{21}$$

where $\hat{S}_l$ is the filtered particle strain rate tensor, of norm $|\hat{S}_l|^2 = 2\hat{S}_{l,ij}\hat{S}_{l,ij}$. The model constants have been evaluated in *a priori* tests [59] leading to the values $C_{S,l} = 0.02$, $C_{V,l} = 0.012$. The final set of equations for the gaseous and the dispersed phases is summarized in Table 1.

Note that the LES model does not explicitly take into account sub-grid scale velocity fluctuations in the calculation of the drag force.

2.6 Numerical Approach

The solver used for this study is a parallel fully compressible code for turbulent reacting two-phase flows, on both structured and unstructured grids. The fully ex-

Gas velocity	$\frac{\partial \bar{\rho} \tilde{u}_i}{\partial t} + \frac{\partial \bar{\rho} \tilde{u}_i \tilde{u}_j}{\partial x_j} = -\frac{\partial \bar{P}}{\partial x_i} + \frac{\partial \tilde{\tau}_{ij} + \tau_{ij}^t}{\partial x_j} - F_{d,i} + \hat{u}_{l,i}\Gamma$
Mass fractions	$\frac{\partial \bar{\rho} \tilde{Y}_k}{\partial t} + \frac{\partial \bar{\rho} \tilde{u}_j \tilde{Y}_k}{\partial x_j} = -\frac{\partial \tilde{J}_k + J_k^t}{\partial x_j} + \dot{\omega}_k^t + \delta_{kF}\Gamma, \text{ for } k = 1, N$
Gas total energy	$\frac{\partial \bar{\rho} \tilde{E}}{\partial t} + \frac{\partial \bar{\rho} \tilde{u}_j \tilde{E}}{\partial x_j} = \frac{\partial (\tilde{\tau}_{ij} + \tau_{ij}^t)\bar{u}_i}{\partial x_j} - \frac{\partial \tilde{q}_j + q_j^t}{\partial x_i} + \Phi + \tilde{u}_i(-F_{d,i} + \hat{u}_{l,i}\Gamma) + \dot{\omega}_T^t$
(non chemical)	
Number density	$\frac{\partial \bar{n}_l}{\partial t} + \frac{\partial \hat{u}_{l,j} \bar{n}_l}{\partial x_j} = 0$
Liquid volume fraction	$\frac{\partial \rho_l \bar{\alpha}_l}{\partial t} + \frac{\partial \hat{u}_{l,j} \rho_l \bar{\alpha}_l}{\partial x_j} = -\Gamma$
Liquid velocity	$\frac{\partial \rho_l \bar{\alpha}_l \hat{u}_{l,i}}{\partial t} + \frac{\partial \rho_l \bar{\alpha}_l \hat{u}_{l,i} \hat{u}_{l,j}}{\partial x_j} = F_{d,i} - \hat{u}_{l,i}\Gamma + \frac{\partial \bar{\tau}_{l,ij}^t}{\partial x_j}$
Enthalpy	$\frac{\partial \rho_l \bar{\alpha}_l \hat{h}_{s,l}}{\partial t} + \frac{\partial \rho_l \bar{\alpha}_l \hat{u}_{l,i} \hat{h}_{s,l}}{\partial x_j} = -(\Phi + \Gamma h_{s,F}(\check{T}_l))$

Table 1: Set of (6+N) conservation equations, where N is the number of chemical species.

plicit finite volume solver uses a cell-vertex discretisation with a Lax-Wendroff centred numerical scheme [60] or a third order in space and time scheme named TTGC [61]. Characteristic boundary conditions NSCBC [10, 62] are used for the gas phase. Boundary conditions are easier for the dispersed phase, except for solid walls where particles may bounce off. In the present study it is simply supposed that the particles stick to the wall, with either a slip or zero velocity.

As pointed out in section 2, high velocity and number density gradients may appear, and are difficult to handle with centered schemes. However the simulations presented in this paper run smoothly thanks to at least four reasons:
(1) In the different cases, RUM is not so strong anyway because the small droplets tend to align with the gas flow and the light load avoids particle-particle and particle-wall interactions, that are the main sources of RUM.
(2) In the combustion chamber application, evaporation reduces the numerical stiffness of the problem as it decreases even more the droplet size and the load.
(3) The simulations are all run in the LES framework, i.e. calculating filtered (and

15

by definition smoothened) quantities and introducing sub-grid scale turbulent viscosities.

(4) As is classical with centered schemes, artificial viscosity is used. This is done with great care to preserve accuracy, applying it very locally (using specific sensors) and with the minimum level of viscosity [40].

3   One-dimensional laminar two-phase flame

As the final application is combustion chambers, it is crucial to check that the model correctly handles flames. In this context, the one-dimensional two-phase flame burning liquid fuel (Fig. 3) is a classical and mandatory test case. Depending on inlet conditions, two different cases are possible: either the evaporation and reaction zones are separated (homogeneous flame), or they are overlapping (heterogeneous flame) [63, 64]. In the present case and for validation purposes only homogeneous flames are considered. This means that in a steady configuration, the flame must be located at a distance D from the injection allowing complete evaporation, i.e. $D \geq D_c = s_l t_{evap}$ where t_{evap} is the evaporation time that may be estimated from the d^2-law for evaporation.

Following [63,64], if the evaporation and combustion zones are separated, it is possible to build an analytical solution that will serve as a reference. The derivation assumes a constant Spalding number B, a constant and uniform liquid temperature T_l in the droplets, the same velocity $\mathbf{u}$ for both phases, a constant pressure P, and constant C_p, λ and ρD_F. For this validation case, the fuel is JP10 ($C_{10}H_{16}$), a kerosene surrogate, which is modelled using a simple one-step chemical scheme:

$$C_{10}H_{16} + 14O_2 \rightarrow 10CO_2 + 8H_2O \tag{22}$$
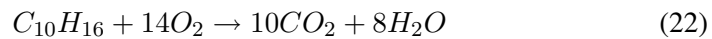
The chemical model follows an Arrhenius law with a pre-exponential factor $A = 6.454 \; 10^{13}$ cgs and the activation energy $E_a = 29189$ cal/mol. These coefficients

16
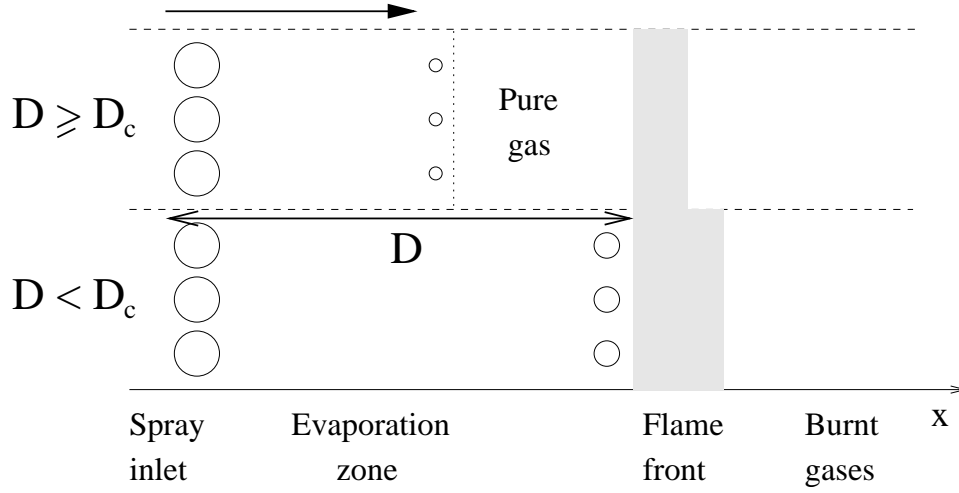
Figure 1: Sketch of the 1D-flame test case: top - homogeneous flame, bottom - heterogeneous flame.

have been adjusted with a genetic algorithm [65] starting from a reduced chemistry [66], to fit flame speed and thickness for lean premixed flames at atmospheric pressure. Fig. 2 shows how this scheme performs compared to a full chemical scheme for JP10 for lean mixtures.

In the two-phase flame, pure liquid fuel is injected with a droplet diameter of $d = 20\ \mu m$ and a volume fraction of $\alpha_l = 4.867\ 10^{-5}$, corresponding to a stoichiometric ratio of $\phi = 0.7$. For this value of ϕ the flame speed of the JP10 flame is 0.49 m/s. The evaporation time being of the order of 6.67 ms, the flame must be initially placed at a minimal distance of 3.38 mm from the injection point in order to stay homogeneous.

Fig. 3 and 4 show a comparison of the computed flame and the reference so- lution for the liquid volume fraction and the droplet diameter, as well as mass and heat exchange terms. The agreement between the two solutions is very good. Only a slight difference is observed in the evaporation zone, as the reference solution is calculated with a constant liquid temperature whereas a variable liquid temperature

17

is computed in the LES code.
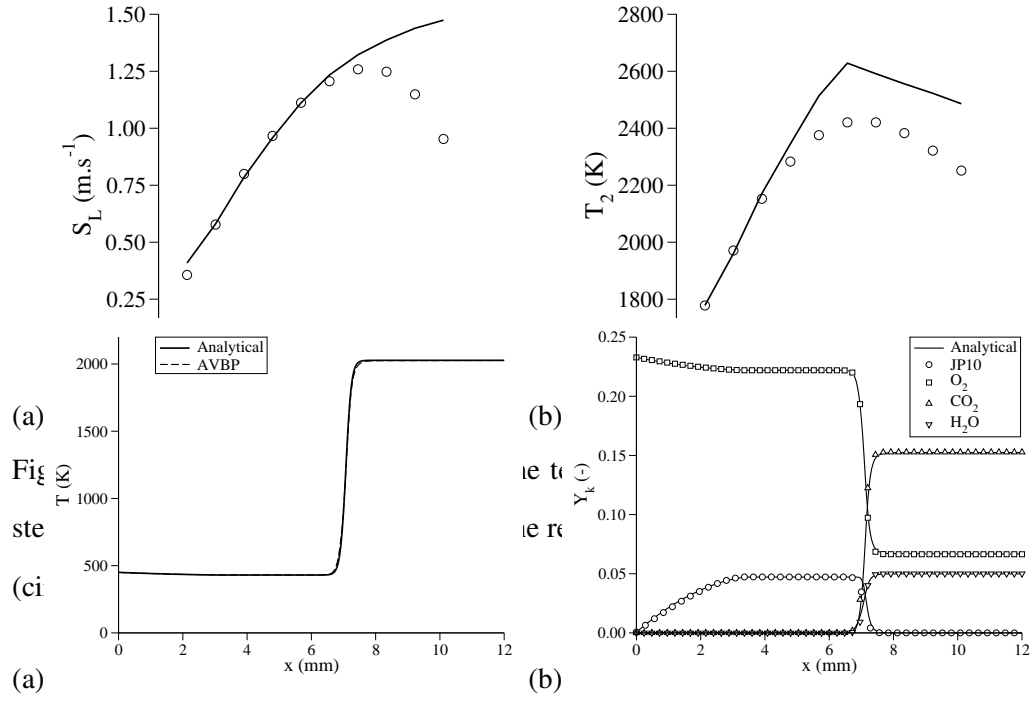
Figure 3: One-dimensional two-phase flame: comparison between the analytical solution and the calculation. (a) Gas temperature (b) Mass fractions.
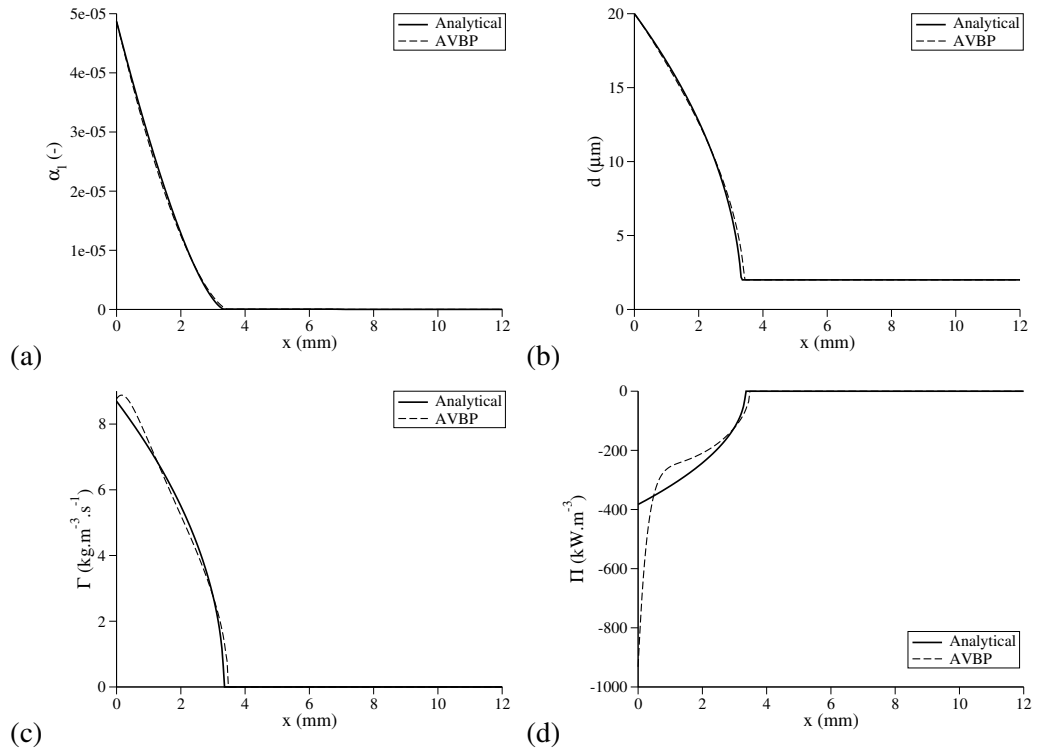
Figure 4: One-dimensional two-phase flame: comparison between the analytical solution and the calculation. (a) Liquid volume fraction (b) Diameter (c) Mass transfer (d) Heat transfer

19

4 Turbulent dispersion

A second validation is related to turbulent dispersion of the particles. Many experiments on turbulent dispersion of particles are reported in the literature, but only a few give enough detailed results to be used for comparison with LES and validation of the numerical method [67–69]. In the present work the experiment of Sommerfeld and Qiu [1] has been chosen as it is a well-known test case for two-phase-flows and provides a significant amount of data. This configuration has already been simulated with the EL approach on a refined mesh by Apte [70]. Our objective is to evaluate the performance of the EE approach and the associated models in the framework of LES with coarser grids.

The configuration (Fig. 5) is a simple pipe, with a swirling co-axial injection. The Plexiglas tube is 1.5 m long with an inner diameter of 194 mm. Dust particles are injected through the primary flow (inner pipe of the injector), with a mean diameter of 45 μm and a size spectrum between 15-80 μm. The secondary annular flow is swirled with a swirl number of 0.47 (calculated as the ratio of the axial flux of angular momentum to the axial flux of linear momentum, integrated over the injector section), resulting in a central annular recirculation zone. Particle size and velocity as well as particle size-velocity correlations were measured at several cross-sections using PDA. Although a polydisperse particle distribution was used in the experiment, monodisperse results are available using size-conditioned averages. The Euler-Euler simulation is performed for particles of 45 μm and compared to the same class of droplets used in the experiment. As for the dilute flows in gas turbines, particle-particle interactions and two-way coupling are negligible in this experiment so that statistics obtained for a single class can be compared to experimental data. The corresponding Stokes number based on the particle relaxation time and the flow time scale (outside the recirculation zone) is of the order of 2.2. Sommerfeld and Qiu [1] define a second Stokes number that is more relevant to

Air flow	
Mass flow rate of the primary jet (g/s)	9.9
Mass flow rate of the secondary jet (g/s)	38.3
Temperature (K)	300

Particles	
Mass flow rate (g/s)	0.34
Mass loading	0.034
Temperature (K)	300
Size distribution (μm)	15-80

Table 2: Flow conditions for the Sommerfeld configuration.

the recirculation zone that leads to smaller values, of the order of 0.2 for particles of 45 μm. Table 2 summarizes flow conditions and particle properties.

The simulation domain (Fig. 5) includes a portion of the inlet pipes (length 50 cm), the full test section and the stagnation chamber. The mesh (Fig. 5) contains 753,000 nodes, corresponding to 4,114,000 cells. It has a smallest cell size of 0.5 mm and is refined in the near-injector region. This leads to a CPU cost of 15 hours on a Compaq AlphaServer with 55 processors, for 40 ms of simulated physical time. The simulation uses a Smagorinsky sub-grid scale model for the gas and the model of Moreau [59] for the liquid. At the pipe inlet, fluctuating turbulent velocities are prescribed on both the gas and the liquid phases [47] to reproduce the inlet turbulence levels measured in the experiment.

Fig. 6 gives a global view of an instantaneous two-phase flow solution. The opening of the jet is clearly visible as well as the recirculation zone for both phases. After injection, the droplets travel first at the same velocity as the gas, but are trapped by the recirculation zone around the stagnation region. In this zone the
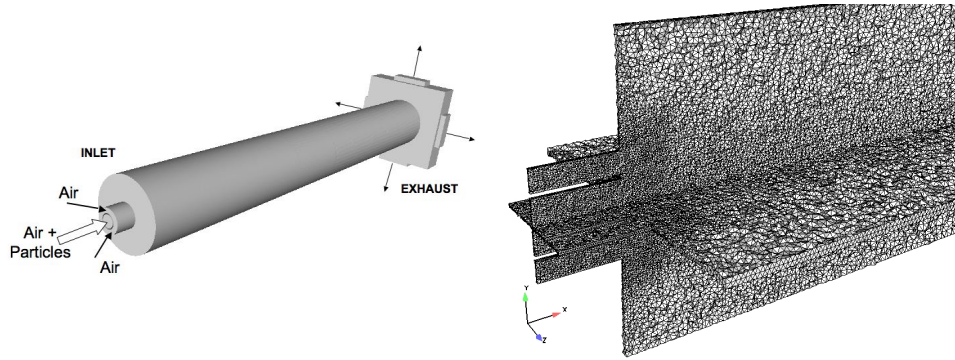
Figure 5: Computational domain and mesh of the Sommerfeld configuration.

droplets accumulate and the number density increases strongly.
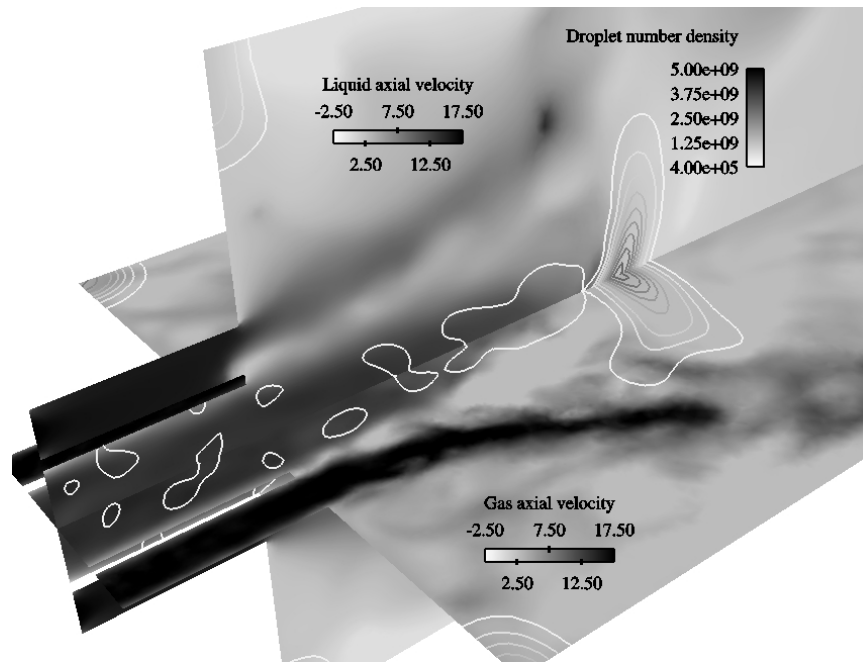
Figure 6: View of the instantaneous two-phase flow in the Sommerfeld configuration: vertical plane: liquid axial velocity; horizontal plane: gas axial velocity; isolines: droplet number density.

Figs. 7 and 8 show the gaseous mean velocity components (axial and tangen-

22

tial) and Figs. 9 and 10 show their RMS values, at different axial positions. The
agreement between the simulation results and the measurements is very good, for
both mean and fluctuating values, and up to the plane located furthest downstream.
In particular the location and thickness of the shear layer are well reproduced by
the simulation, both features that are known to be difficult to predict and demon-
strate the quality of the present calculation. The recirculation zone is also well
captured, at the correct location around $100\ mm$ downstream the injector nozzle.
This is confirmed by the results on fluctuating velocities, showing that not only the
level but also the shape of the profiles are well captured.

The same velocity profiles are plotted for the liquid phase on Figs. 11 to 14.
Two experimental results are plotted, corresponding to either the data conditionned
on the single droplet size of $45\ \mu m$ or to the data averaged on all droplet sizes.
Results show that the effect of polydispersion on the mean velocity is weak, except
near the stagnation zone induced by the recirculation where the polydispersion has
a tendency to delay the velocity decrease. As for the gas phase, the numerical
solution for the mean velocity is in good agreement with experimental data. The
main discrepancy is again near the stagnation zone, known to be difficult to predict,
and seems to indicate that the recirculation zone is too close from the injection
plane. However velocity profiles do not give a complete view of the flow structure
and the comparison between the numerical and experimental 3D flow fields (Fig. 6)
shows that the structures of the flow and of the recirculation zone are well captured
by the simulation. Compared to experiment, fluctuating velocity profiles are also
well captured in shape, but are underestimated by the simulation. This was also
observed in [47, 50] and is due to the missing RUM, that represents a significant
part of the particle sub-grid scale motion. Finally the liquid mass flow rate shown
on Fig. 15 indicates a correct numerical prediction of the liquid phase, with only a
reduced flux decrease along the axis due to the discrepancy between the velocities
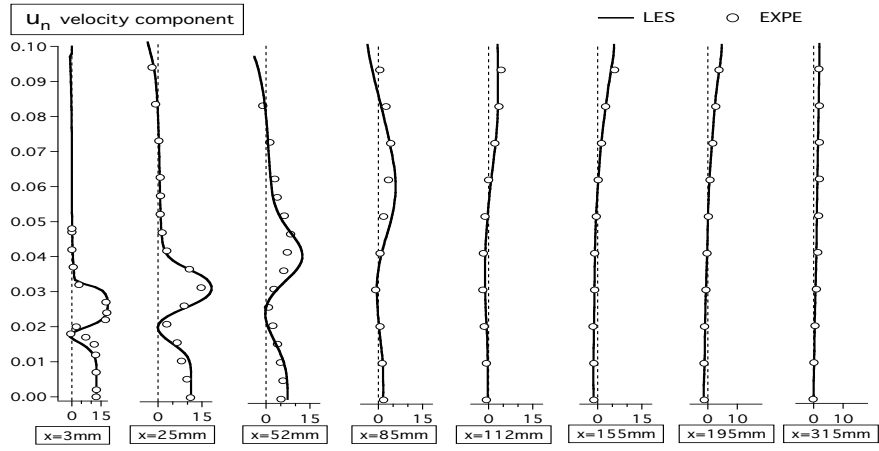
Figure 7: Mean axial velocity profiles for the gas phase.
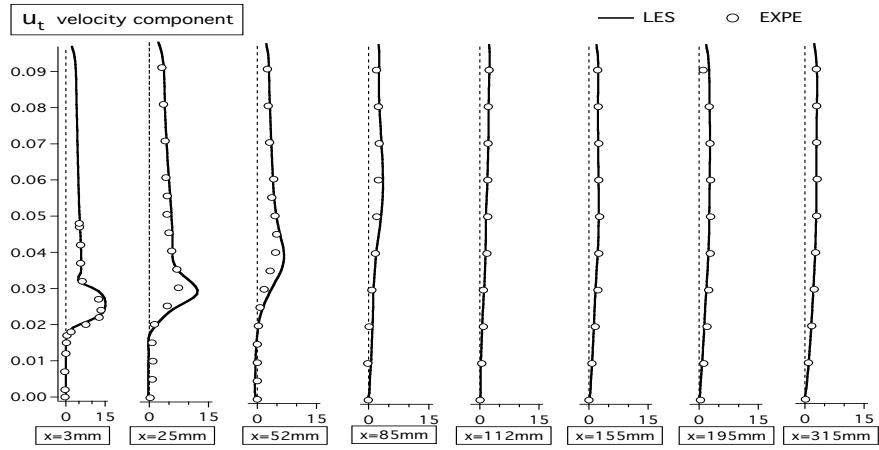
Figure 8: Mean tangential velocity profiles for the gas phase.

already observed in the same region.
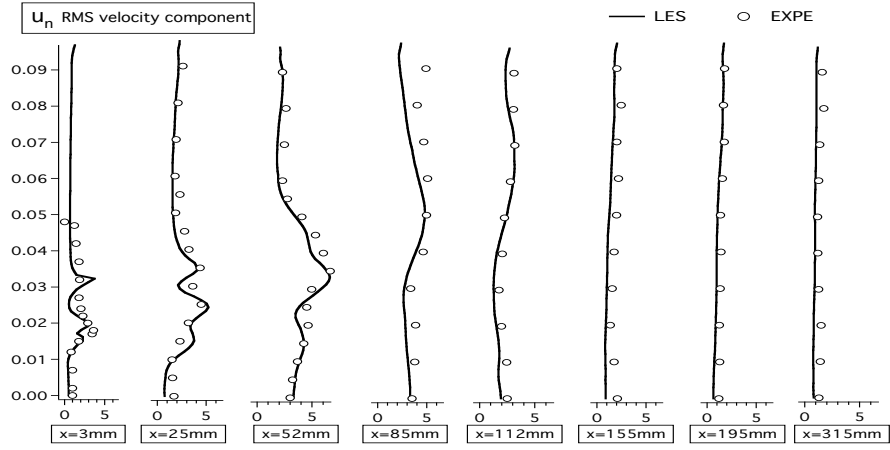
Figure 9: RMS axial velocity profiles for the gas phase.
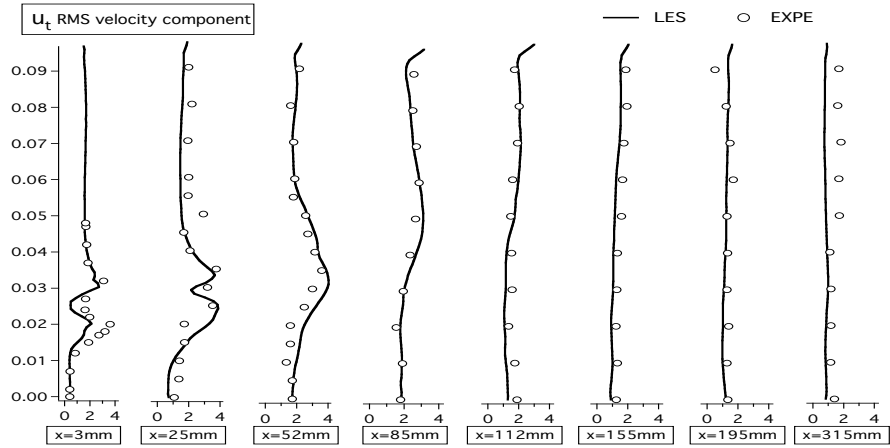
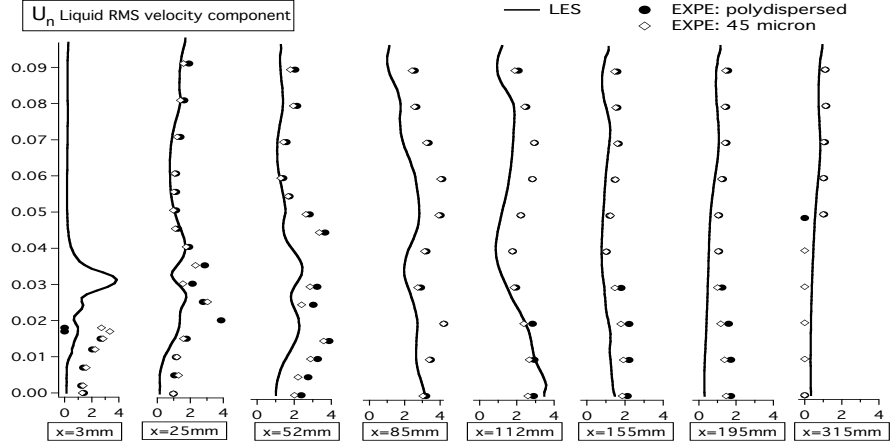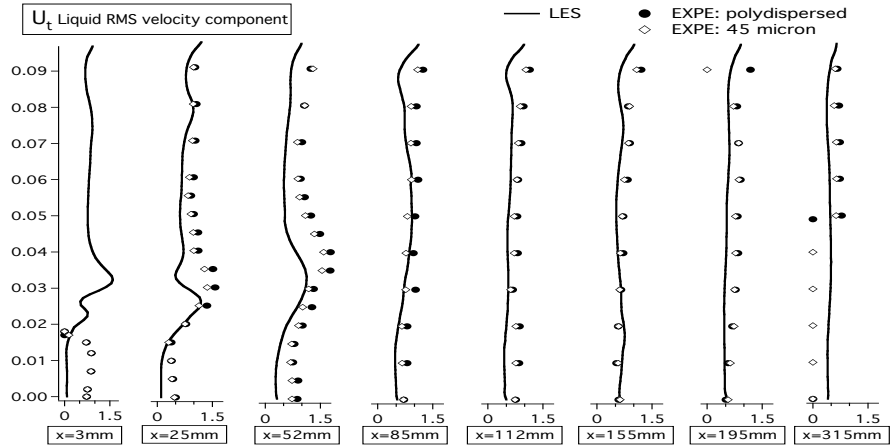Figure 10: RMS tangential velocity profiles for the gas phase.

25
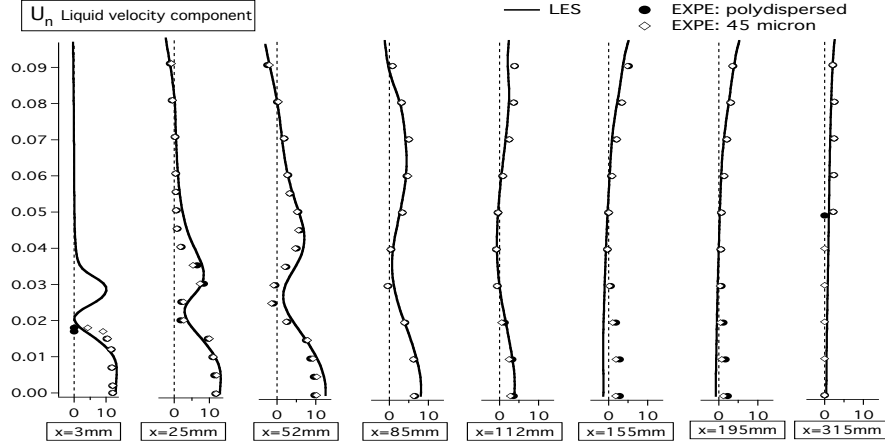
Figure 11: Mean axial velocity profiles for the liquid phase. Numerical simulations use 45 μm monodisperse droplets.
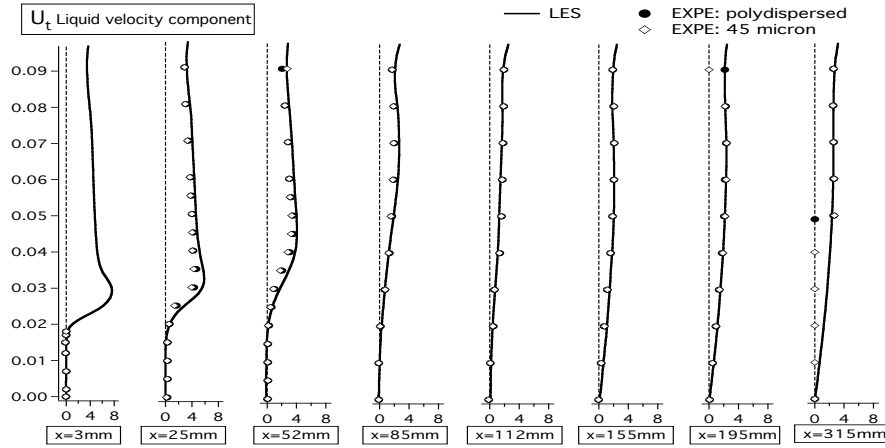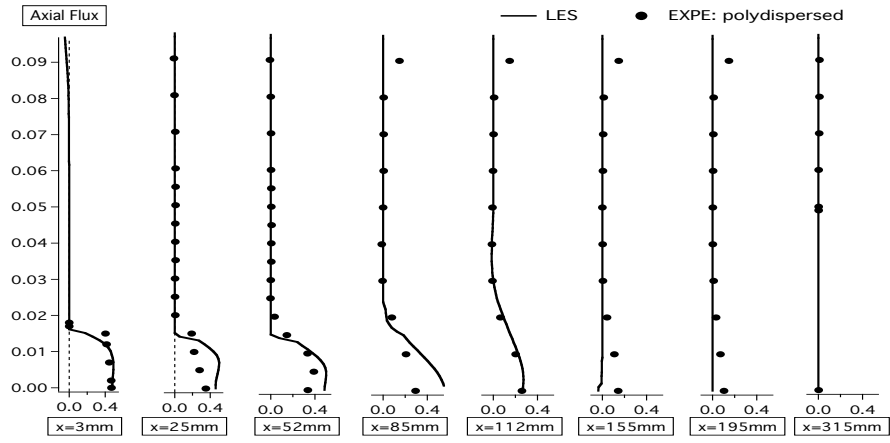

Figure 12: Mean tangential velocity profiles for the liquid phase. Numerical simulations use 45 μm monodisperse droplets.

Figure 13: RMS axial velocity profiles for the liquid phase. Numerical simulations use $45\ \mu m$ monodisperse droplets.

Figure 14: RMS tangential velocity profiles for the liquid phase. Numerical simulations use $45\ \mu m$ monodisperse droplets.

Figure 15: Axial liquid mass flux. Numerical simulations use 45 μm monodisperse droplets.

5   Reacting flow in an aircraft combustion chamber

5.1   Configuration

The last test case is a 3D sector of 22.5-degrees of an annular combustor at atmospheric pressure. The kerosene Liquid Spray (*LS*) is located at the center of the main Swirled Inlet (SI) (Fig. 17). Small Holes (H), located around the inlet aim at lifting the flame and protect the injector from high temperatures. The perforations localized on the upper and lower walls are divided in two parts. The Primary Jets (PJ) bring cold air to the flame in the first part of the combustor where combustion takes place. The Dilution Jets (DJ) inject air further downstream to reduce and homogenise the outlet temperature to protect the turbine. The Spark Plug (SP) is located under the upper wall between two (PJ) (Fig. 18). The geometry (Fig. 19) also includes cooling films which protect walls from the flame.

The inlet and outlet boundary conditions use characteristic treatments with relaxation coefficients to reduce acoustic reflexion [10, 71]. The SI imposed velocity field mimics the swirler influence. Figure 16 displays profiles of the three compo- nents of the air velocity as prescribed along the axis of the spray (AB on Fig. 19) in reduced units: $u^* = u/U_0$ as a function of $r^* = r/R_0$ where U_0 is the bulk velocity and R_0 is the radius of the SI. The other inlets are simple jets. The injected spray is monodisperse, composed of droplets of diameter of $15\ \mu m$ leading to a Stokes number, based on the droplet relaxation time and the swirl flow time of 0.57. The volume fraction, $\alpha_l \simeq 10^{-3}$, is imposed for a disk of radius $r^* = 0.4$. This corresponds to a lean global stoichiometric ratio of 0.28. At injection, the liquid velocity is equal to the gaseous velocity as the droplet Stokes number is lower than one. The droplet inlet temperature equals $288\ K$ and the air is at $525\ K$. No-slip conditions are used on the upper and lower walls while a symmetry condition

Air flow	
Total mass flow rate (g/s)	119
Temperature (K)	525
Pressure (bar)	1

Liquid fuel	
Mass flow rate (g/s)	2.38
Temperature (K)	300
Droplet size (μm)	15

Table 3: Flow conditions for the gas turbine configuration.

is used on the sector sides. All conditions are summarized in Table 3.

The unstructured mesh is composed of 400,000 nodes and 2,300,000 tetrahedra, which is typical and reasonable for LES of such configuration. The explicit time step is $\Delta t \simeq 0.22 \ \mu s$. The mesh is refined close to the inlets and in the combustion zone (Fig. 20), leading to a flame thickening factor of the order of 10. The one-step chemical scheme described in section 3 is used here without any changes. It has been checked that in the simulation the flame mostly burns mixtures with an equivalence ratio in the range between 0.5 and 1, where the chemical scheme is valid.

5.2 Steady spray flame

First a steady turbulent two-phase flame is calculated. The $15 \ \mu m$ droplet motion follows the carrier phase dynamics so that the Centered Recirculation Zones (CRZ) are similar for gas and liquid, as illustrated on Fig. 21, showing the in- stantaneous backflow lines of both phases, plotted in the vertical central cutting
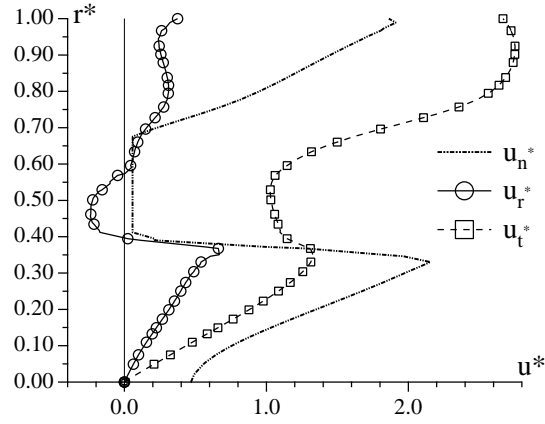
Figure 16: Normal, radial and tangential injection velocity profiles for the burner configuration: $r^* = r/R_0$ and $u^* = u/U_0$ where R_0 and U_0 are respectively the SI radius and the bulk velocity.
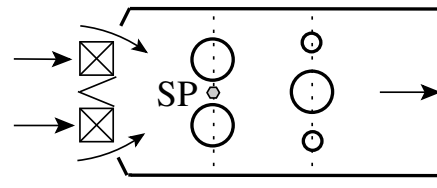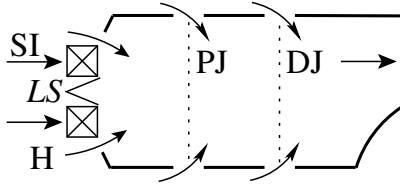
Figure 17: Geometry sketch : side view   Figure 18: Geometry sketch : top view
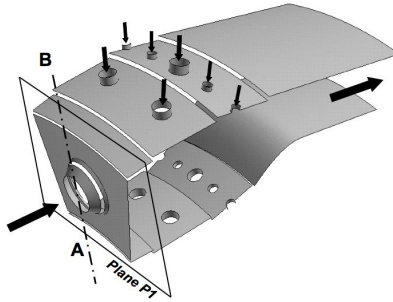
Figure 19: Chamber geometry   Figure 20: Mesh view on central plane
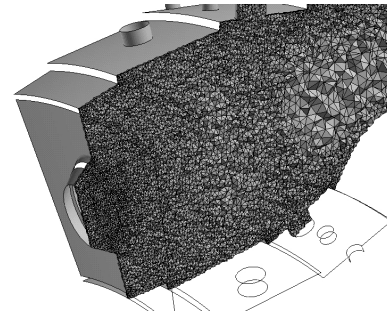
plane. Maintained by this CRZ, the droplets accumulate and the droplet number density, presented with the liquid volume fraction field on Fig. 21, rises above its

initial value: a zone where the droplet number density n_l is larger than $2n_{l,inj}$ (where $n_{l,inj}$ is its value at injection) is formed downstream of the injector at a distance approximately half of the nozzle diameter (lines with circles on Fig 21). The increased residence time of these droplets, whose diameter field is presented on Fig. 22, increases the local equivalence ratio distribution. The heat transfer linked to the phase change leads to the reduction of the gaseous temperature, as shown by the isoline $T = 450\ K$ on Fig. 23, and an increase of the dispersed phase tem- perature. Thus, the CRZ, by trapping evaporating droplets, stabilises the vaporised fuel and the flame. The flame front visualized on Fig. 23 by the heat release field
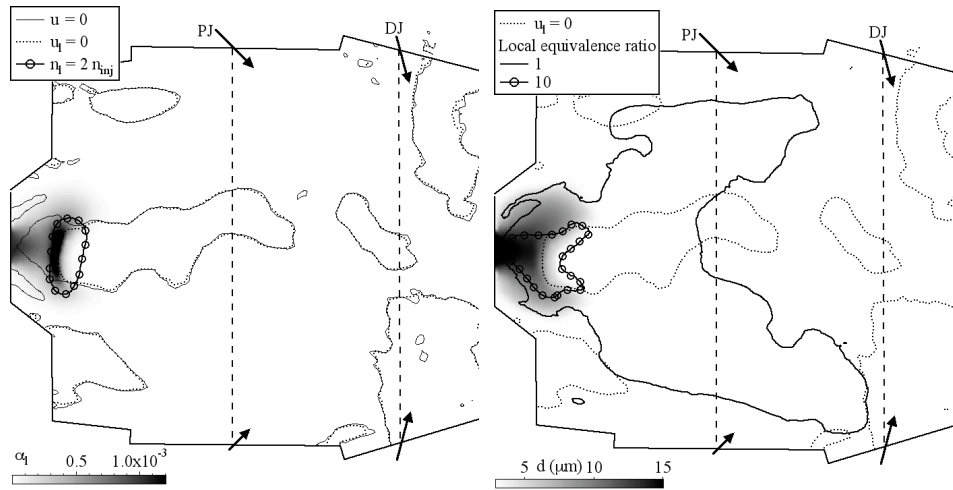
Figure 21: Instantaneous field of volume fraction in the central cutting plane of the chamber, with zero-velocity lines and $n_l = 2n_{inj}$ isoline.

Figure 22: Instantaneous field of droplet diameter in the central cutting plane of the chamber, with equivalence ratio isolines for the values 1 and 10.

is influenced by both flow dynamics and evaporation rate. The main phenomena controlling flame stabilisation are :

1. the air velocity must be low enough to match the turbulent flame velocity :

the dynamics of the carrier phase (and in particular the CRZ) stabilises the flame front on a stable pocket of hot gases

2. zones where the local mixture fraction is within flammability limits must exist : combustion occurs between the fuel vapour radially dispersed by the swirl and the ambient air, where the equivalence ratio is low enough

3. the heat release must be high enough to maintain evaporation and reaction : the sum of heat flux Π and heat release $\dot{\omega}_T$, plotted on Fig. 23, allows to iden- tify the zone (—) where the heat transfer due to evaporation compensates the local heat release : $\Pi + \dot{\omega}_T = 0$.

In the present case, the flame front is stabilised by the CRZ (1) but the heat release magnitude is reduced in the evaporation zone because of both effects (2) and (3). To determine the flame regime (premixed and/or diffusion), the Takeno index $\mathcal{T} = \nabla Y_F . \nabla Y_O$ and an indexed reaction rate $\dot{\omega}_F^* = \dot{\omega}_F \frac{\mathcal{T}}{|\nabla Y_F|.|\nabla Y_O|}$ are used [72]. The flame structure is then divided into two parts : $\dot{\omega}_F^* = +\dot{\omega}_F$ in the premixed regime and $\dot{\omega}_F^* = -\dot{\omega}_F$ in the diffusion regime (Fig. 24). In the primary zone, the partially premixed regime dominates because of the unsteady inhomogeneous fuel vapour. In the dilution zone, the unburned fuel reacts with dilution jets through a diffusion flame, as confirmed by the coincidence between the flame and the stoichiometric line.

In his review on vortex breakdown, Lucca-Negro [73] classifies the hydrodynamic instabilities appearing in swirled flows. For high swirl numbers, the axial vortex breaks down at the stagnation point S and a spiral is created around a central recirculation zone CRZ (Fig. 25) : this vortex breakdown is the so-called Precess- ing Vortex Core (PVC) and occurs in a large number of combustors [74]. LES captures the vortex breakdown in the combustor and its frequency is evaluated with the backflow line on a transverse plane (Fig. 26) at six successive times marked with
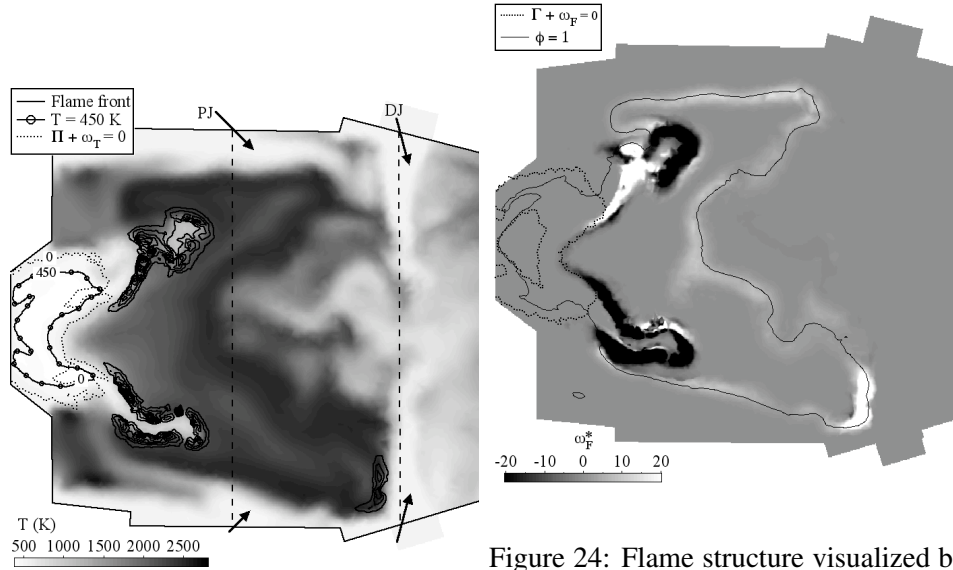
Figure 23: Flame front

Figure 24: Flame structure visualized by the indexed reaction rate. Black zones correspond to premixed flames and white zones to diffusion flames.

a number from 1 to 6 and separated by 0.5 ms. The turnover time is estimated at $\tau_{PVC} \simeq 3.5$ ms, corresponding to a frequency of $f_{PVC} \simeq 290$ Hz. Moreover, the three rotating motions of the SI, the whole PVC structure and the spiral winding turn in the same direction, as illustrated by the rotating arrows on Fig. 25. The PVC defined on Fig. 27a controls the motions of both the Vaporised Fuel (VF) zone and the flame front. Fig. 27b displays the temperature field, the maximum fuel mass fraction (white lines) and the flame front (black isolines of reaction rate $\dot{\omega}_F$). In the cutting plane, defined on Fig. 27a, the CRZ stabilises hot gases and enhances evaporation leading to a cold annular zone where the maximum fuel mass fraction precesses. The flame motion follows the PVC and the reaction rate is driven by the fuel vapour concentration.
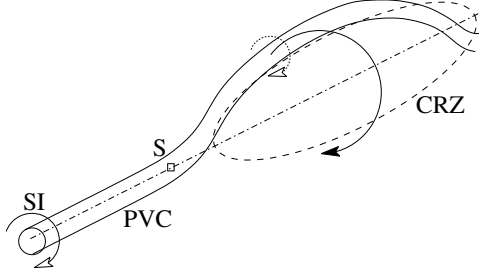
Figure 25: Precessing Vortex Core.
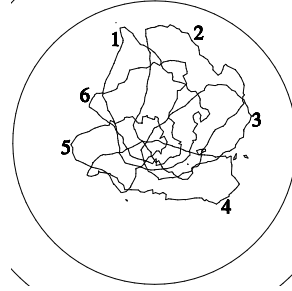
Figure 26: Backflow line : transverse cut in plane P1 (Fig 19).
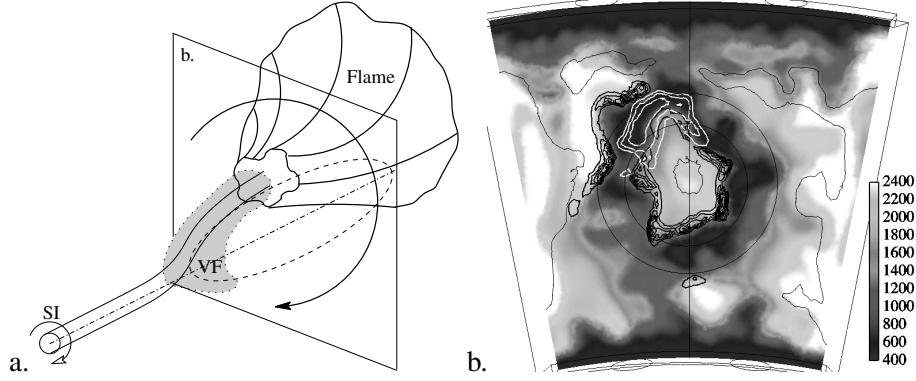
Figure 27: PVC influence on evaporation and combustion (left). Fields of temperature and isolines of fuel vapor (white lines) and reaction rate (black lines) (right).

5.3 Ignition sequence

Ignition sequences can also be simulated with the same LES tool. The numerical method used to mimic an ignition by spark plug in the combustion chamber is the addition of the source term $\dot{\omega}_{spark}$ in Eq. (23). This source term, defined by Eq. (23), is a gaussian function located at (x_0, y_0, z_0) near the upper wall between both primary jets and deposited at time $t = t_0 = 0$. The spark duration, typical of industrial spark plugs, is $\sigma_t = 0.04 \; ms$. The total deposited energy is $E_{spark} =$

$150\ J$.

$$\dot{\omega}_{spark} = \frac{E_{spark}}{(2\pi)^2 \sigma_t \sigma_r{}^3} e^{-\frac{1}{2}\left[\left(\frac{t-t_0}{\sigma_t}\right)^2 + \left(\frac{x-x_0}{\sigma_r}\right)^2 + \left(\frac{y-y_0}{\sigma_r}\right)^2 + \left(\frac{z-z_0}{\sigma_r}\right)^2\right]} \tag{23}$$

The temporal evolution of the total (i.e. spatially integrated) power deposited by the spark is presented on Fig. 28, along with the total heat release $\dot{\omega}_T$ and the spatially averaged temperature. After a heating phase due to the source term on the energy equation (up to approximately $0.08\ ms$), the temperature is sufficient to initiate the reaction between fuel vapour and air, leading to a sudden increase of the heat release of the exothermic reaction. When the spark is stopped (at $\approx 0.18\ ms$), the total heat release decreases, and finally stabilizes at a level corresponding to a propagating flame, while the mean temperature continues to increase: the ignition is successful.
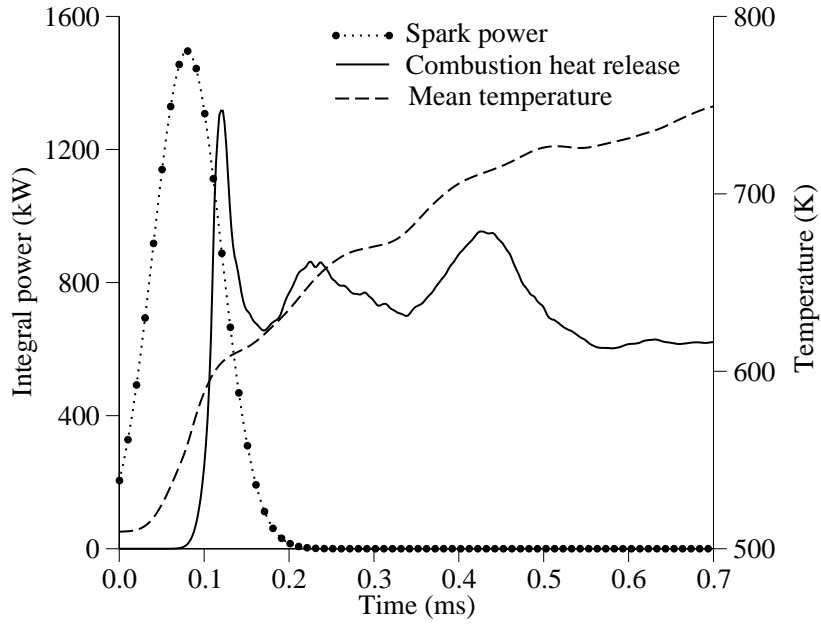
Figure 28: Total (spatially integrated) source term $\dot{\omega}_{spark}$, total heat release $\dot{\omega}_T$, and spatially averaged temperature.

The transition from the ignition of the first flame kernel ($t = 0.2\ ms$) to a complete stabilisation takes more time (more than $3\ ms$) and is illustrated on the longitudinal central cutting plane identified in Fig. 29 with the fuel mass fraction field and the reaction rate isolines. The first image is presented at $t = 0.2\ ms$ and after, successive images are separated by $\Delta t = 0.2\ ms$. At the beginning of the computation, the 15 μm droplets evaporate in the ambient air at $T = 525\ K$ creating a turbulent cloud of vaporised fuel in the whole primary zone. This fuel vapour is trapped by the CRZ and is transported from the evaporation zone to the spark plug area. At $t = 0$, the spark ignition leads to the creation of a hot kernel. The propagation of the flame front created by this pocket of hot gases is highly controlled by the fuel vapour distribution between $t = 0$ and $t = 1\ ms$. After $t = 0.2\ ms$, this flame loses its spherical shape due to convective effects. The downstream side of the flame front is blown away and extinguishes by lack of fuel while the bottom side is progressing towards the center line where the fuel vapour concentration is high. When entering the CRZ ($t = 1\ ms$), the front is strongly wrinkled by the large turbulent scales of the flow. However, in the upstream region of the CRZ, the low velocities enable to stabilize the edge of the reacting zone close to the fuel injection ($t = 1$ to $1.4\ ms$). In this region, the flame and the back-flow maintain a high temperature ambient leading to a strong evaporation rate and creating a stable fuel vapour concentrated spot ($t = 1.6$ to $2.4\ ms$). Due to the swirled jet, this fuel vapour is radially dispersed into the air flow and produce a flammable mixture. Burning this mixture, the flame is able to spread in the radial direction and finally occupies a large section of the primary zone ($t = 2.4\ ms$). This last topology corresponds to the steady spray flame described in the previous section.

This ignition sequence shows the important role of the liquid phase, responsible for the great differences with the ignition of a purely gaseous flame. The

controlling mechanism is evaporation, that delays the start of the chemical reaction and, together with the droplet turbulent dispersion, modifies the fuel vapor distribution and consequently the flame front propagation. This was never visualized and, despite the use of simplified models, the simulation provides a good and new qualitative description of the phenomena.
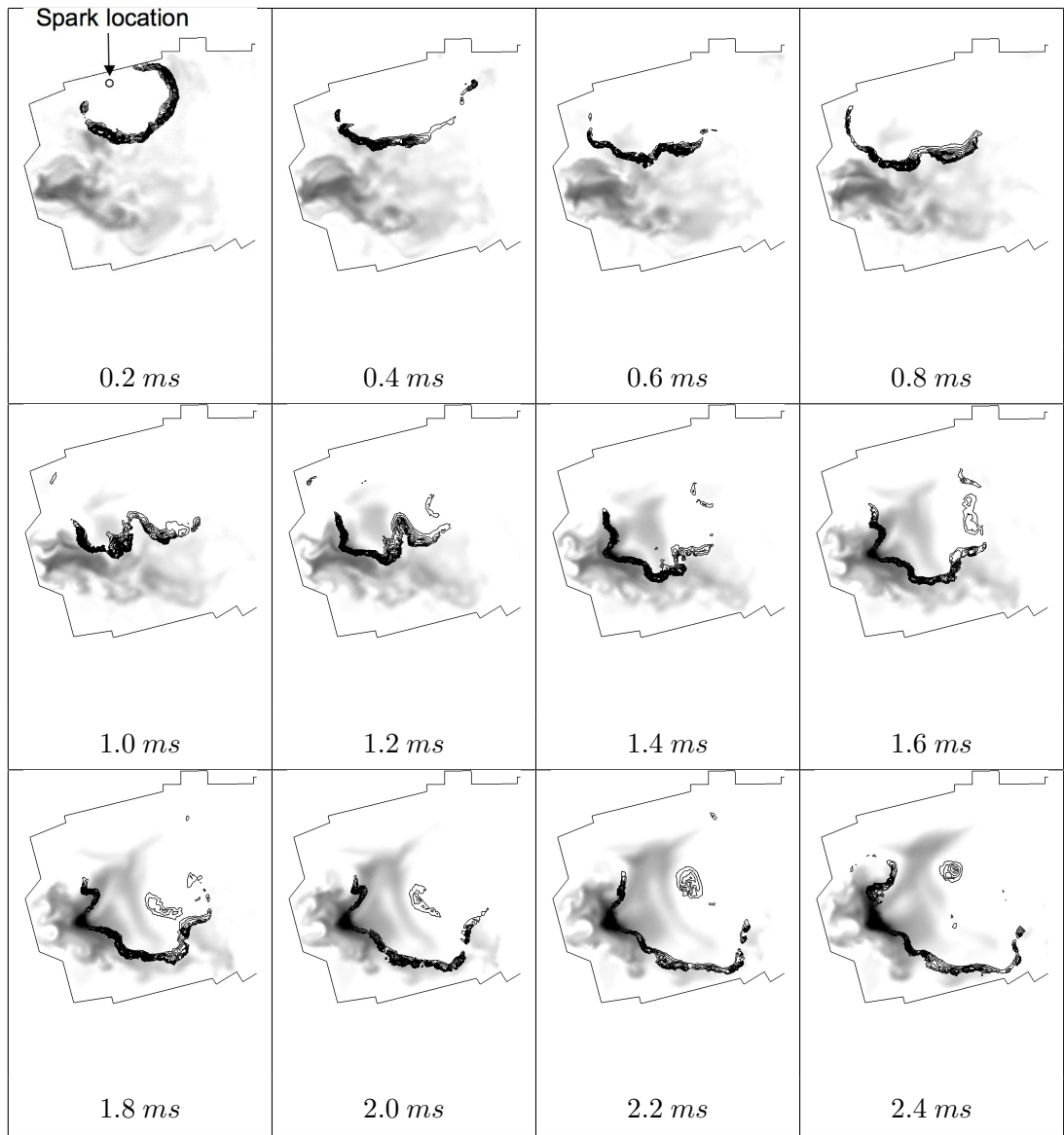
Figure 29: Flame front propagation on fuel mass fraction field (white: 0 → black: 0.35)

6 Conclusions

A steady spray flame in a realistic aeronautical combustor has been computed using a parallel LES Euler/Euler solver. This approach was first tested in two simple reference cases: a one-dimensional laminar two-phase flame of JP10 with air and a swirled non-reacting flow with solid particles [1]. The influence of the dispersed phase on the flame motion has been highlighted, in particular the role of the evaporation process. The unsteady approach brings new insight into the physics of such complex reactive two-phase flows. Furthermore, it allows the computation of an ignition sequence from the formation of the first spherical flame front to the stabilisation of the turbulent spray flame. Obviously more quantitative comparisons of the present method with existing Euler-Lagrange methods and with experiments (such as [47]) are needed. But this paper shows that despite its limitations and still open modelling issues, the Euler-Euler approach already leads to interesting results on the tested configurations and demontrates its feasability and capabilities for two-phase flow combustion.

References

[1] M. Sommerfeld and H. H. Qiu. Characterisation of particle-laden, confined swirling flows by phase-doppler anemometry ad numerical calculation. *Int. J. Multiphase Flow*, 19(6):1093–1127, 1993.

[2] D. Caraeni, C. Bergstrom, and L. Fuchs. Modeling of liquid fuel injection, evaporation and mixing in a gas turbine burner using large eddy simulation. *Flow Turb. and Combustion*, 65:223–244, 2000.

[3] V.K. Chakravarthy and S. Menon. Subgrid modeling of turbulent premixed flames in the flamelet regime. *Flow Turb. and Combustion*, 65:133–161, 2000.

[4] O. Colin, F. Ducros, D. Veynante, and T. Poinsot. A thickened flame model for large eddy simulations of turbulent premixed combustion. *Phys. Fluids*, 12(7):1843–1863, 2000.

[5] H. Forkel and J. Janicka. Large-eddy simulation of a turbulent hydrogen diffusion flame. *Flow Turb. and Combustion*, 65(2):163–175, 2000.

[6] H. Pitsch and L. Duchamp de la Geneste. Large eddy simulation of premixed turbulent combustion using a level-set approach. *Proc of the Comb. Institute*, 29:2001–2005, 2002.

[7] K. Mahesh, G. Constantinescu, and P. Moin. A numerical method for large-eddy simulation in complex geometries.

[8] L. Selle, G. Lartigue, T. Poinsot, R. Koch, K.-U. Schildmacher, W. Krebs, B. Prade, P. Kaufmann, and D. Veynante. Compressible large-eddy simulation of turbulent combustion in complex geometry on unstructured meshes. *Combust. Flame*, 137(4):489–505, 2004.

[9] Y. Sommerer, D. Galley, T. Poinsot, S. Ducruix, F. Lacas, and D. Veynante. Large eddy simulation and experimental study of flashback and blow-off in a lean partially premixed swirled burner. *J. of Turbulence*, 5, 2004.

[10] V. Moureau, G. Lartigue, Y. Sommerer, C. Angelberger, O. Colin, and T. Poinsot. High-order methods for DNS and LES of compressible multi-component reacting flows on fixed and moving grids. *J. Comput. Phys.*, 202(2):710–736, 2005.

[11] S. Roux, G. Lartigue, T. Poinsot, U. Meier, and C. Bérat. Studies of mean and unsteady flow in a swirled combustor using experiments, acoustic analysis and large eddy simulations. *Combust. Flame*, 141:40–54, 2005.

[12] T. Poinsot and D. Veynante. *Theoretical and numerical combustion*. R.T. Edwards, 2nd edition., 2005.

[13] A.H. Lefebvre. *Gas Turbines Combustion*. Taylor & Francis, 1999.

[14] C. Weber and Z. Angrew. The decomposition of a liquid jet. *Math. Mech.*, 11:136–154, 1931.

[15] S. Nukiyama and Y. Tanasawa. Experiments in on the atomization of liquids in air stream. report 3 : on the droplet-size distribution in an atomized jet. *Trans. Soc. Mech. Eng. Japan*, 5:62–67, 1939.

[16] R. D. Reitz and F. V. Bracco. Mechanism of atomization of a liquid jet. *Physics of Fluids*, 25(10):1730–1742, 1982.

[17] Z. Han, S. Parrish, P.V. Farrell, and D. Reitz. Modeling atomization processes of pressure-swirl hollow-cone fuel sprays. *Atomization and Sprays*, (6):663–684, 1997.

[18] J.C. Lasheras and E.J. Hopfinger. Liquid jet instability and atomisation in a coaxial gas stream. *Ann. Rev. Fluid. Mech.*, 32:275–308, 2000.

[19] S.V. Apte, K. Mahesh, P. Moin, and J.C. Oefelein. Large-eddy simulation of swirling particle-laden flow in a coaxial combustor. *International Journal of Multiphase Flow*, 29:1311–1331, 2003.

[20] V.M. Alipchenkov and L.I. Zaichik. Modeling of the turbulent motion of particles in a vertical channel. *Journal of Fluid Dynamics*, 41(4):531–544, 2006.

[21] M. Boivin, K. Squires, and O. Simonin. On the prediction of gas-solid flows with two-way coupling using large eddy simulation. *Phys. Fluids* , 12(8), 2000.

[22] B. Oesterlé and L.I. Zaichik. On lagrangian time scales and particle dispersion modeling in equilibrium turbulent shear flows. *Physics of Fluids*, 16(9):3374–3384, 2004.

[23] C. Marchioli, M. Picciotto, and A. Soldati. Particle dispersion and wall-dependent turbulent flow scales: implications for local equilibrium models. *Journal of Turbulence*, 7(60):1–12, 2006.

[24] M. Benson, T. Tanaka, and J.K. Eaton. Effects of wall roughness on particle velocities in a turbulent channel flow. *Journal of Fluids Engineering*, 127(2):250–256, 2005.

[25] M. Sommerfeld and J. Kussin. Analysis of collision effects for turbulent gas-particle flow in a horizontal channel. Part (ii). integral properties and validation. *International Journal of Multiphase Flow*, 29(4):701–718, 2003.

43

[26] I. Gökalp, C. Chauveau, C. Morin, B. Vieille, and M. Birouk. Improving dropelt breakup and vapoization models by including high pressure and turbulence effects. *Atomiztion and Sprays*, 10:475–510, 2000.

[27] V. Sankaran and S. Menon. Les of spray combustion in swirling flows. *J. of Turbulence*, 3:011, 2002.

[28] K. Mahesh, G. Constantinescu, S. Apte, G. Iaccarino, F. Ham, and P. Moin. Progress towards large-eddy simulation of turbulent reacting and non-reacting flows in complex geometries. In *Annual Research Briefs*, pages 115–142. Center for Turbulence Research, NASA Ames/Stanford Univ., 2002.

[29] S. V. Apte, M. Gorokhovski, and P. Moin. Large-eddy simulation of atomizing spray with stochastic modeling of secondary breakup. In *ASME Turbo Expo 2003 - Power for Land, Sea and Air*, Atlanta, Georgia, USA, 2003.

[30] F. Ham, S. V. Apte, G. Iaccarino, X. Wu, M. Herrmann, G. Constantinescu, K. Mahesh, and P. Moin. Unstructured les of reacting multiphase flows in realistic gas turbine combustors. In *Annual Research Briefs*. Center for Turbulence Research, 2003.

[31] H. Enwald, E. Peirano, and A.-E. Almstedt. Eulerian two-phase flow theory applied to fluidization. *Int. J. Multiphase Flow*, 22:21–66, 1996.

[32] E. Peirano and B. Leckner. Fundamentals of turbulent gas-solid flows applied to circulating fluidized bed combustion. *Prog. Energy Comb. Sci.* , 24:259–296, 1998.

[33] J. Gao, C. Xu, S. Lin, and G. Yang. Simulations of gas-liquid-solid 3-phase flow and reaction in FCC riser reactors. *AIChE Journal*, 47(3):677–692, 2001.

[34] A.K. Das. *Computational fluid dynamics simulation of gas-solid risers : reactive flow modelling*. PhD thesis, Universiteit Gent, 2002.

[35] A. Gobin, H. Neau, O. Simonin, J.-R. Linas, V. Reiling, and J.-L. Sélo. Fluid dynamic numerical simulation of a gas phase polymerization reactor. *Int. J. of Numerical Methods in Fluids*, 43:1199–1220, 2003.

[36] P. Moin. Large eddy simulation of multi-phase turbulent flows in realistic combustors. *Prog. in Computational Fluid Dynamics*, 4:237–240, 2004.

[37] A Kaufmann. *Vers la simulation des grandes échelles en formulation Euler/Euler des écoulements réactifs diphasiques*. PhD thesis, INPT, 2004.

[38] P. Février, O. Simonin, and K. Squires. Partitioning of particle velocities in gas-solid turbulent flows into a continuous field and a spatially uncorrelated random distribution: Theoretical formalism and numerical study. *J. Fluid Mech.*, 533:1–46, 2005.

[39] J.B. Mossa. *Extension polydisperse pour la description Euler/Euler des écoulements diphasiques réactifs*. PhD thesis, INP Toulouse, 2005.

[40] E. Riber. *Développement de la méthode de simulation aux grandes échelles pour les écoulements diphasiques turbulents*. PhD thesis, INP Toulouse, 2007.

[41] P. Fede and O. Simonin. Numerical study of the subgrid fluid turbulence effects on the statistics of heavy colliding particles. *Phys. Fluids* , 18(045103), 2006.

[42] P. Fede, P. Villedieu, O. Simonin, and K.D. Squires. Stochastic modeling of the subgrid fluid velocity fluctuations seen by inertial particles. In *Proc of the Summer Program*. Center for Turbulence Research, NASA Ames/Stanford Univ., 2006.

[43] M. Moreau, B. Bedat, and O. Simonin. From euler-lagrange to euler-euler large eddy simulation approaches for gas-particle turbulent flows. In *ASME Fluids Engineering Summer Conference*. ASME FED, 2005.

[44] E. Riber, M. Moreau, O. Simonin, and B. Cuenot. Towards large eddy simulation of non-homogeneous particle laden turbulent gas flows using euler-euler approach. In *11th Workshop on Two-Phase Flow Predictions*, Merseburg, Germany, 2005.

[45] O.A. Druzhinin and S. Elghobashi. On the decay rate of isotropic turbulence laden with microparticles. *Phys. Fluids* , 11(3), 1999.

[46] S. Chapman and T.G. Cowling. *The Mathematical Theory of Non-Uniform Gases*. Cambridge University Press, cambridge mathematical library edition, 1939 (digital reprint 1999).

[47] E. Riber, M. García, V. Moureau, H. Pitsch, O. Simonin, and T. Poinsot. Evaluation of numerical strategies for LES of two-phase reacting flows. In *CTR Summer Program*, Center for Turbulence Research, NASA AMES, Stanford University, USA, 2006.

[48] D.B. Spalding. The combustion of liquid fuels. In *4th Symp. (Int.) on Combustion*. The Combustion Institute, Pittsburgh, 1953.

[49] A. Kaufmann, O. Simonin, T. Poinsot, and J. Helie. Dynamics and dispersion in eulerian-eulerian DNS of two phase flow. In *Proceeding of the Summer Program*, pages 381–391, Center for Turbulence Research, NASA AMES/Stanford University, USA, 2002.

[50] E. Riber, M. Moreau, O. Simonin, and B. Cuenot. Development of Euler-Euler LES approach for gas-particle turbulent jet flow. In *ASME - European Fluids Enigneering Summer Meeting*, 2006.

[51] F. Nicoud and F. Ducros. Subgrid-scale stress modelling based on the square of the velocity gradient. *Flow Turb. and Combustion* , 62(3):183–200, 1999.

[52] J.-Ph. Légier, T. Poinsot, and D. Veynante. Dynamically thickened flame large eddy simulation model for premixed and non-premixed turbulent combustion. In *Summer Program 2000*, pages 157–168, Center for Turbulence Research, Stanford, USA, 2000.

[53] C. Martin, L. Benoit, Y. Sommerer, F. Nicoud, and T. Poinsot. Les and acoustic analysis of combustion instability in a staged turbulent swirled combustor. *AIAA Journal* , 44(4):741–750, 2006.

[54] P. Schmitt, T.J. Poinsot, B. Schuermans, and K. Geigle. Large-eddy simulation and experimental study of heat transfer, nitric oxide emissions and combustion instability in a swirled turbulent high pressure burner.

[55] A. Sengissen, A. Giauque, G. Staffelbach, M. Porta, W. Krebs, P. Kaufmann, and T. Poinsot. Large eddy simulation of piloting effects on turbulent swirling flames. *In Proc. of the Combustion Institute*, 31, 2007.

[56] P. Moin, K. Squires, W. Cabot, and S. Lee. A dynamic subgrid-scale model for compressible turbulence and scalar transport. *Phys. Fluids* , A 3(11):2746–2757, 1991.

[57] B. Vreman, B. Geurts, and H. Kuerten. Subgrid modeling in LES of compressible flow. *Appl. Sci. Res.*, 54:191–203, 1995.

[58] A. Yoshizawa. Statistical theory for compressible turbulent shear flows, with the application to subgrid modeling. *Phys. Fluids* , 29(7):2152–2164, 1986.

[59] M. Moreau, B. Bedat, and O. Simonin. A priori testing of subgrid stress models for euler-euler two-phase LES from euler-lagrange simulations of

gas-particle turbulent flow. In *18th Ann. Conf. on Liquid Atomization and Spray Systems*. ILASS Americas, 2005.

[60] C. Hirsch. *Numerical Computation of internal and external flows*. John Wiley, New York, 1988.

[61] O. Colin and M. Rudgyard. Development of high-order Taylor-Galerkin schemes for unsteady calculations. *J. Comput. Phys.* , 162(2):338–371, 2000.

[62] T. Poinsot and S. Lele. Boundary conditions for direct simulations of compressible viscous flows. *J. Comput. Phys.* , 101(1):104–129, 1992.

[63] T. H. Lin, C. K. Law, and S. H. Chung. Theory of laminar flame propagation in off-stoichiometric dilute sprays. *Int. J. of Heat and Mass transfer*, 31:1023–1034, 1988.

[64] T. H. Lin and Y. Y. Sheu. Theory of laminar flame propagation in near-stoichiometric dilute sprays. *Int. J. of Heat and Mass transfer*, 84:333–342, 1991.

[65] C. Martin. Eporck user guide v1.8. Technical report, CERFACS, 2004.

[66] S.C. Li, B. Varatharajan, and F.A. Williams. Chemistry of jp-10 ignition. *AIAA Journal*, 39(12):2351–2356, 2001.

[67] K. Hishida, K. Takemoto, and M. Maeda. Turbulent characteristics of gas-solids two-phase confined jet. *Japanese Journal of Multiphase Flow*, 1(1):56–69, 1987.

[68] K. Squires and J. Eaton. Measurements of particle dispersion obtained from direct numerical simulations of isotropic turbulence. *J. Fluid Mech.* , 226:1–35, 1991.

[69] J. S. Vames and T. J. Hanratty. Turbulent dispersion of droplets for air flow in a pipe. *Experiments in Fluids*, 6(2):94–104, 2004.

[70] S. V. Apte, K. Mahesh, and T. Lundgren. A eulerian-lagrangian model to simulate two-phase/particulate flows. In *Annual Research Briefs*. Center for Turbulence Research, 2003.

[71] L. Selle, F. Nicoud, and T. Poinsot. The actual impedance of non-reflecting boundary conditions: implications for the computation of resonators. *AIAA Journal*, 42(5):958–964, 2004.

[72] H. Yamashita, M. Shimada, and T Takeno. A numerical study on flame stability at the transition point of jet diffusion flame. In *26th Symp. (Int.) on Combustion*, pages 27 – 34. The Combustion Institute, Pittsburgh, 1996.

[73] O. Lucca-Negro and T. O'Doherty. Vortex breakdown: a review. *Prog. Energy Comb. Sci.*, 27:431–481, 2001.

[74] L. Selle. *Simulation aux grandes échelles des couplages acoustique / combustion dans les turbines á gaz*. Phd thesis, INP Toulouse, 2004.

List of Figures

List of Tables